Applied Catalysis A: General 453 (2013) 383–390

Contents lists available at SciVerse ScienceDirect

Applied Catalysis A: General

journal homepage: www.elsevier.com/locate/apcata

Microwave-assisted catalysis by iron oxide nanoparticles on MCM-41: Effect of the support morphology

Adela I. Carrillo[a], Elena Serrano[a], Rafael Luque[b,*], Javier García-Martínez[a,**]

[a] Molecular Nanotechnology Lab., Department of Inorganic Chemistry, University of Alicante, Carretera San Vicente s/n, E-03690 Alicante, Spain
[b] Dpto. Química Orgánica, Universidad de Córdoba, Campus de Rabanales, Edif. Marie Curie, Ctra. Nnal. IV, Km 396, E14014 Córdoba, Spain

ARTICLE INFO

Article history:
Received 15 September 2012
Received in revised form
11 December 2012
Accepted 16 December 2012
Available online 4 January 2013

Keywords:
Microwaves
Heterogeneous catalysis
Iron oxide nanoparticles
MCM-41 type materials

ABSTRACT

Catalytically active heterogeneous catalysts have been prepared via microwave deposition of iron oxide nanoparticles (0.5–1.2 wt%) on MCM-41 type silica materials with different morphologies (particles, helical and spheres). This methodology leads to iron oxide nanoparticles composed by a mixture of FeO and Fe_2O_3 species, being the Fe(II)/Fe(III) peak ratio near to 1.11 by XPS. DRUV spectroscopy indicates the presence of tetrahedral coordinated Fe^{3+} in the silica framework of the three catalysts as well as some extraframework iron species in the catalysts with particle and sphere-like morphologies. The loading of the nanoparticles does neither affect the mesopore arrangement nor the textural properties of the silica supports, as indicated by SAXS and nitrogen adsorption/desorption isotherms. A detailed investigation of the morphology of the supports in various microwave-assisted catalyzed processes shows that helical mesostructures provide optimum catalytic activities and improved reusabilities in the microwave-assisted redox (selective oxidation of benzyl alcohol) catalyzed process probably due to a combination of lower particle size and higher acidity in comparison with the supports with particle and sphere morphology.

1. Introduction

The beginning of the Green Chemistry era from the fundamental development of principles and methods [1,2] steered chemistry research groups to focus their efforts in searching for novel and innovative synthetic pathways which are also more efficient and environmentally friendly. Metal nanoparticles (MNPs) are one of the areas in nanotechnology that have attracted much attention over the past decade due to their high chemical activities and specificities of interaction [3]. However, in many cases MNPs are unstable due to their high surface energy because of the high surface area/volume ratio [4–6]. A promising research avenue proposed to stabilize nanoparticles is related to the use of porous supports (e.g. mesoporous silicas)[7–9].

In general, the stabilization of MNPs on porous supports can be achieved by two different methodologies. Traditionally, preformed porous supports, including mesoporous silica, are employed to stabilize MNPs on their surface or within their porous framework. Such loading is generally carried out using a wide variety of techniques including impregnation, co-precipitation, sonication and others [10,11].

An alternative approach entails the co-precipitation of the silica source and the selected functionality modified with tri-alkoxysilane terminal groups. By using this approach, Garcia-Martinez et al. [12,13] have recently developed a novel methodology to incorporate several functionalities (i.e. metal nanoparticles, coordination complexes, molybdenum cluster or acid/redox sites) in mesoporous silica and organosilica supports.

Microwave-assisted protocols have been recently studied for the loading of metal nanoparticles on the surface or within the framework of porous materials, being a promising alternative to overcome inherent drawbacks of unsupported nanoparticles in terms of stability, agglomeration and reusability. Luque et al. [11] recently reported an efficient and greener method to obtain highly active and well-dispersed SBA-15 supported MNPs (Au, Ag, Pd and Ru) based on a microwave-assisted route, followed by the first report of directly prepared catalytically active low-loaded supported Fe-NPs (i.e. 0.3 wt%) by extending the microwave-assisted approach to the preparation of highly active Fe_2O_3 nanoparticles supported on a MCM-41 silica [18]. None of these reports investigated any particular insights into the morphology of the support which has been reported to be as important as its internal structure [12,13]. As example, MCM-41-like particle shape materials including mesoporous silica nanoparticles [14], ordered hollow spheres [15], helical mesoporous silica [16], mesoporous silica fibers [17],

* Corresponding author. Tel.: +34 957212065; fax: +34 957212066.
** Corresponding author. Tel: +34 965 903400x2224; fax: +34 965943454.
E-mail addresses: q62alsor@uco.es (R. Luque), j.garcia@ua.es (J. García-Martínez).

0926-860X/$ – see front matter © 2013 Elsevier B.V. All rights reserved.
http://dx.doi.org/10.1016/j.apcata.2012.12.041

or spheres with a core-shell structure [12] have been investigated as nanoparticles supports proving in many cases that the design and careful selection of an optimum morphology in a solid support is a key step in the development of a more efficient and reusable catalyst for heterogeneously catalyzed processes from the green chemistry standpoint.

This contribution is aimed to prepare highly active and selective iron oxide nanoparticles supported on MCM-41 type silica materials with various morphologies ranging from conventional MCM-41 to helical mesostructured materials (HMM) [13] and interconnected core-shell silica spheres (ISS) [12a]. The final goal is to study their activities in heterogeneously catalyzed processes and the influence of the morphology on their final properties. The selection and design of an optimum support for the iron oxide NPs has therefore been combined with the efficiency of microwaves to achieve a green route to high added value products (e.g. benzaldehyde, diphenylmethane) in some relevant processes including the selective oxidation of benzyl alcohol to benzaldehyde and Friedel-Crafts alkylations of toluene with benzyl chloride.

2. Experimental

2.1. Materials

Tetraethylorthosilicate (TEOS, 98%), octadecyltrimethylammonium bromide (C_{18}TAB, >99%), cetyltrimethylammonium bromide (C_{16}TAB, 96%) and $FeCl_2.4H_2O$ (99%) were used as silica source, structure-directing agents and iron source, respectively. Aqueous ammonia solution (NH_4OH, 30%) was used in the synthetic protocol to obtain MCM-41 type materials. All chemicals were purchased from Aldrich and used as received without further purification.

2.2. Synthesis of the mesoporous supports

Mesoporous supports were synthesized by hydrothermal synthesis procedure, according to our previous reported synthesis [13]. The synthetic conditions are listed in Table 1.

2.2.1. Synthesis of conventional MCM-41: MCM-41

Our reported synthesis of MCM-41 type silicas [13] was followed to prepare the mesoporous silica materials with a conventional morphology. In a typical synthesis, 0.44 g of C_{16}TAB were dissolved in a 35 mM NH_4OH solution (41.92 ml) at 313 K. 2.33 ml TEOS was then added to the surfactant solution. The molar composition of the synthesis gel was 1 SiO_2:0.12 C_{16}TAB:1.41 NH_4OH:280 H_2O. The solution was then transferred to a 100 ml Teflon lined stainless steel autoclave and heated at 353 K under hydrothermal conditions for 24 h. After cooling to room temperature, the solid product was first washed with water and then with ethanol, filtered off, and air-dried overnight. Finally, the surfactant was removed by calcination at 823 K for 8 h (2 K/min) under static air atmosphere.

2.2.2. Synthesis of MCM-41 type materials with a helical morphology: HMM

The helical mesoporous silica materials, HMM, were synthesized in a similar way to the MCM-41 materials described above but using vigorous stirring and high ammonia concentration, as recently reported elsewhere [13]. The composition of the synthesis gel obtained was 1 SiO_2:0.12 C_{16}TAB:90 NH_4OH:490 H_2O.

2.2.3. Synthesis of MCM-41 spheres with a core-shell structure: ISS

Well-ordered mesoporous interconnected silica spheres, ISS, were prepared following a similar procedure to the MCM-41 materials synthesis. In this case, the synthesis was carried out with high ammonia concentration and extremely low surfactant amount (i.e. a surfactant/silica molar ratio of 0.03 instead of the classical surfactant/silica molar ratio of 0.12) [13]. The molar composition of the synthesis gel was 1 TEOS:0.03 C_{18}TAB:60 NH_4OH:466 H_2O. As previously reported [12], the use of hexadecyltrimethylammonium bromide (C_{16}TAB) as surfactant instead of C_{18}TAB does not lead to the desired morphology.

2.3. Deposition of supported iron oxide nanoparticles into the silica supports

Supported iron oxide nanoparticles were obtained using a microwave-assisted methodology previously developed by Luque et al. for the preparation of supported metal and metal oxide nanoparticles on mesoporous materials [18]. In a typical procedure, 0.2 g of the support was suspended in EtOH (2 ml) containing 0.1 g of the iron precursor ($FeCl_2{\cdot}4H_2O$). The mixture was heated in a microwave at 200 W for 15 min. The resulting materials were then filtered off, washed with a methanol excess and acetone and dried overnight to yield a red–orange fine powder.

Materials were denoted as Fe-MCM-41 (for the materials with a conventional MCM-41 morphology), Fe-HMM (for those containing helical morphologies) and Fe-ISS (interconnected silica spheres) [13]. The properties of the as-synthesized catalysts are summarized in Table 1.

2.4. Characterization

The morphology of the mesoporous materials was investigated by Transmission Electron Microscopy (TEM) using a JEM-2010 microscope (JEOL, 200 kV, 0.14 nm of resolution). Samples for TEM analysis were prepared by dipping a sonicated suspension of the sample in ethanol on a carbon-coated copper grid. The digital analysis of the TEM micrographs was performed using DigitalMicrograph™ 3.6.1. by Gatan.

Reflectance UV–vis (DRUV) data of pressed powders were recorded on a UV–vis spectrophotometer AGILENT 8453 with a Harrick praying mantis accessory, in a wavelength range from 200 to 600 nm, and recalculated following the Kubelka Munk function.

The electronic states of iron species in the materials were determined by X-ray photoelectron spectroscopy (XPS) in a VG-Microtech Multilab instrument, using MgK-α radiation of energy 1253.6 eV and a pass energy of 50 eV. The analysis pressure during data acquisition was 5×10^{-7} Pa. A careful deconvolution of the spectra was made and the areas under the peaks were estimated by calculating the integral of each peak after subtracting a Shirley background and fitting the experimental peak to a combination of Lorentzian/Gaussian lines of 30–70% proportions. Binding energies were referenced to the C1s line at 284.6 eV from adventitious carbon [19].

Metal loading in the materials was determined by inductively coupled plasma optical emission spectroscopy (ICP-AES) on a Perkin–Elmer 40 instrument. Samples were digested in 1 ml HF (48 wt% of catalyst) during 12 h, prior to analysis by ICP-AES.

Surface acidity was measured in a dynamic mode with a previously described pulse chromatographic technique involving gas-phase (573 K) adsorption of Py (sum of Brönsted and Lewis acid sites) and DMPy (Brönsted sites) as probe molecules [29]. Very small volumes of solutes were injected to approach the conditions of gas chromatography linearity. The apparatus used for Py adsorption was basically a gas chromatograph, modified by dispensing with the empty column before the catalyst tube which is connected directly to the detector so that the eluted band was recorded directly and peak retardation occurred only on the catalyst. The catalyst tube was made of a 100 mm × mm s.s. tube containing about 200 mg of catalyst packed between quartz wool plugs. Pure helium at a flow rate of 12 ml/min was used as the

Table 1
Synthesis conditions, textural and structural parameters of the mesoporous catalysts, Fe-MCM-41, Fe-HMM and Fe-ISS, as compared to the neat mesoporous silica supports.

Sample	Molar ratio x:y (1 SiO_2:x CTAB:y NH_4OH)	Metal loading[a] (wt%)	Surf. acidity[b] (μmol Py/g)	d_p [c] (nm)	a[d] (nm)	b_d [e] (nm)	A_{BET} [f] (m^2/g)	V_p [g] (cm^3/g)
MCM-41	0.12 C_{16}TAB:1.41 NH_4OH	0	<10	3.00	4.80	1.80	860	0.80
Fe-MCM-41		1.2	33	2.85	4.90	2.05	820	0.78
HMM	0.12 C_{16}TAB:90 NH_4OH	0	<10	2.75	4.70	1.95	1050	0.78
Fe-HMM		0.6	41	2.50	4.20	1.70	905	0.65
ISS	0.03 C_{18}TAB:60 NH_4OH	0	<10	3.40	5.25	1.85	450	0.46
Fe-ISS		0.5	28	3.15	5.25	2.10	450	0.45

[a] Iron amount determined by ICP analyses.
[b] Surface acidity expressed in μmol of pyridine adsorbed per gram of material [28].
[c] Average mesopore diameters were estimated from the adsorption branch of the nitrogen isotherm using the BJH method.
[d] Unit cell parameter, a, obtained by an hexagonal symmetry according to the equation $a = 2/3^{1/2}d_{100}$, from XRD spectra.
[e] Pore wall thickness was estimated by subtracting the pore diameter from the lattice unit parameter ($b_d = a - d_p$).
[f] The BET surface area was estimated by multipoint BET method using the adsorption data in the relative pressure (P/P_0) range of 0.05–0.30.
[g] Mesopore volume from the isotherms at relative pressure of 0.95 (see Section 2).

carrier gas. Before adsorption experiments were started, catalyst was pretreated in situ by passing pure helium, at a flow rate of 12 ml/min, for 323–723 K (rate 10 K/min) and remaining at 723 K for 10 min. After catalyst pre-treatment, the temperature was lowered to the temperature at which the adsorption experiment was carried out (usually 323 K), maintaining the helium flow. Adsorption experiments were carried out in the temperature range 323–523 K. After adsorption at the desired temperature, the weakly held pyridine was then eluted from the catalyst by continuing the stream of helium for an additional 1 h at the temperature at which the adsorption takes place. Then the temperature was lowered to 323 K and thermal desorption experiments carried out from 323 to 723 K at a rate of 10 K/min, remaining at 723 K for 10 min. Desorption was measured by a FID. The GC signal due to pyridine was proportional to the partial pressure above the catalyst surface, which is directly proportional to the desorption of pyridine, because the flushing speed was constant. The integral of the rates was therefore proportional to the amount of pyridine desorbing from one adsorption site. Repeated adsorption/TPD experiments using the same sample did not show any change in the desorption curve.

Small-angle powder X-ray diffraction (XRD) analysis was carried out with a Philips PW3040/00 diffractometer using a CuKα radiation (λ = 1.54056 Å), operating at 40 kV and 30 mA, at a scanning rate of 0.03°/min in the $0.7° < 2\theta < 10°$ range. The unit cell parameter, a, was estimated from the (1 0 0) interplanar spacing accordingly with the symmetry of the pores ($a = 2/3^{1/2}d_{100}$ for a hexagonal symmetry). The pore wall thickness, b_d, for mesoporous materials was estimated by subtracting the pore diameter from the lattice unit parameter ($b_d = a - d_p$) [20]. Spectra in the wide-angle scan (10–80°) were taken in a Bruker D8-Advance diffractometer, operating at 40 kV and 35 mA, at a scanning rate of 2.0°/min, using the same radiation.

Textural properties were determined by N_2 adsorption at 77 K in an AUTOSORB-6 apparatus. Samples were previously degassed for 4 h at 523 K at 5×10^{-5} bars. The adsorption branch was used to determine the pore size distribution using the Barret–Joyner–Halenda (BJH) method. The surface area was determined using the multipoint BET method in the 0.05–0.30 relative pressure ranges. As expected for these materials, the micropore volume, estimated from the t-plot method, was determined to be zero and thus the mesopore volume can be directly read from the isotherms at relative pressure of 0.95. These values are in good agreement with those obtained from the adsorption branch of the nitrogen isotherm using the BJH method, where the volume was measured at the plateau of the cumulative adsorption pore volume plot (approximately 40 nm). Gas adsorption at higher P/P_0 is mainly due to interparticle condensation.

2.5. Catalytic experiments

Microwave experiments were performed on a CEM DISCOVER microwave reactor with PC control and monitored by sampling aliquots of reaction mixture that were subsequently analyzed by GC/GC–MS using an Agilent 6890 N GC model equipped, with a 7683B series autosampler, fitted with a DB-5 capillary column and an FID detector. The microwave method was generally power-controlled where the samples were irradiated with different power outputs (e.g. settings at maximum power, 300 W) to achieve the desired temperature (373 K). Response factors of the reaction products were determined with respect to the original starting materials from GC analysis using known compounds in calibration mixtures of specified compositions.

2.5.1. Microwave-assisted selective oxidation of benzyl alcohol to benzaldehyde

Experiments were conducted under closed vessel mode (pressure controlled) under continuous stirring. In a typical run, 2 mmol benzyl alcohol, 4 mmol H_2O_2 (0.4 ml, 30 wt% in water), 2 ml acetonitrile and 0.05 g catalyst were placed on a microwave CEM-Discover reaction vessel and microwaved for 3 min at 300 W (maximum power output) [18]. The final mixture was then filtered off to separate the catalyst, extracted and subsequently analyzed by GC/GC–MS.

2.5.2. Microwave-assisted alkylation of toluene with benzyl chloride

Experiments were conducted under open vessel mode under continuous stirring. The catalytic alkylation of benzyl chloride was performed as follows: 0.2 ml benzyl chloride, 2 ml toluene and 0.025 g catalyst were placed into a tube and microwaved for 30 min at 300 W (maximum power output) [21]. The final mixture was processes in a similar way as to the oxidation reactions and finally analyzed by GC/GC–MS.

3. Results and discussion

3.1. Catalyst characterization

Table 1 shows the properties of the supported iron oxide nanoparticles, where the metal loading of the different catalysts determined by ICP is also included. As previously observed for both porous and no porous supports [18], this synthetic route leads to a low metal loading, i.e. 0.5–1.2 wt% (Table 1). TEM and DRUV analyses confirm the incorporation of the iron oxide nanoparticles in the silica supports.

Representative TEM micrographs of the Fe-MCM-41, Fe-HMM and Fe-ISS materials are presented in Fig. 1a–c, respectively. TEM

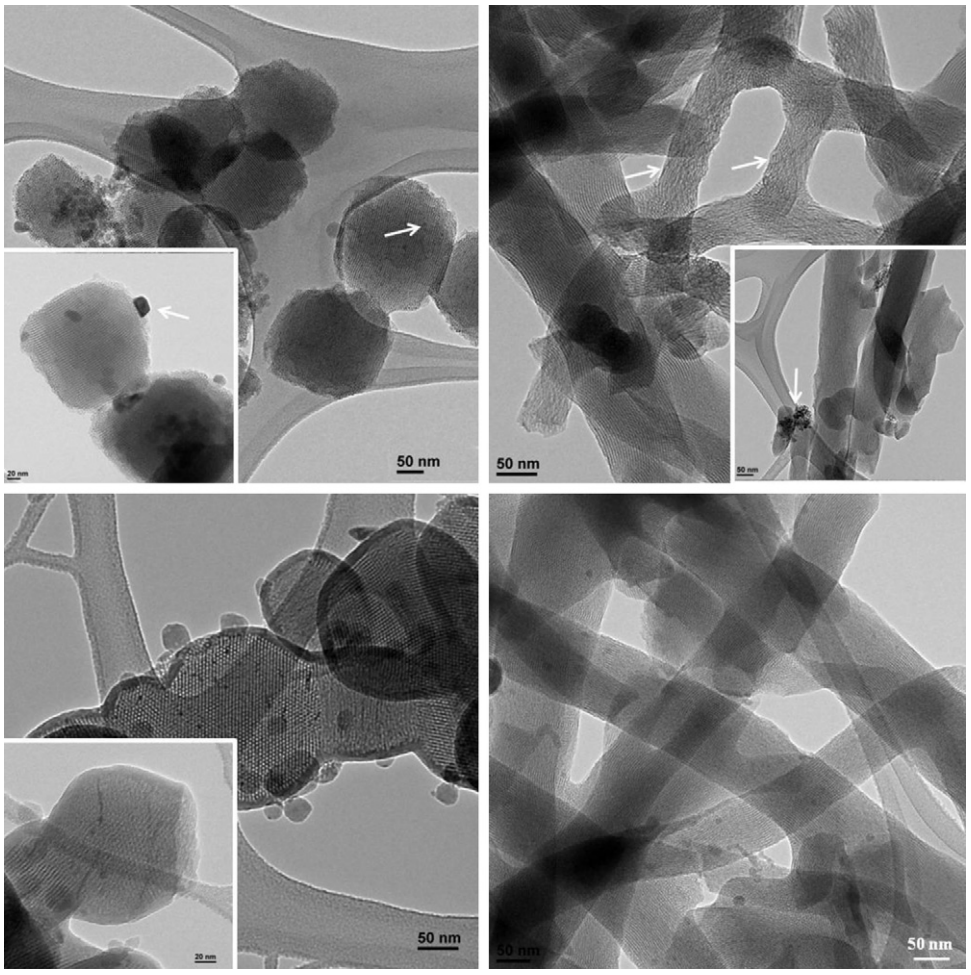

Fig. 1. TEM micrographs of: (a) Fe-MCM-41, scale bar in the inset = 20 nm, (b) Fe-HMM, scale bar in the inset = 50 nm, (c) Fe-ISS, scale bar in the inset = 20 nm and (d) Fe-HMM after has been used as catalyst in the benzyl alcohol oxidation. Arrows point out the iron oxide nanoparticles.

analyses confirm that the morphology of each material is preserved upon incorporation of the iron oxide nanoparticles on the mesoporous supports. Iron oxide nanoparticles are imaged in TEM micrographs as dark spots. Due to the low contrast difference between silica and iron oxide nanoparticles in the microscope, various white arrows are included in the TEM images to help identify the nanoparticles. TEM image of Fe-MCM-41 (Fig. 1a) shows the nanoparticles both inside and outside of the silica structure. Nevertheless, these nanoparticles are mostly incorporated into the silica matrix in Fe-HMM and Fe-ISS type materials (Fig. 1b and c, respectively). The different incorporation of the nanoparticles in the supports, together with their different sizes, leads to a different catalytic behavior of the materials in the investigated reactions.

DRUV spectroscopy confirmed the presence of the iron oxide nanoparticles in the silicas (Fig. 2). For comparison, a DRUV spectrum of the as-synthesized Fe nanoparticles has been included in Fig. 2 (entry Fe-NPs). As expected, the supports show little or no absorbance in the analyzed range. Fe-HMM exhibited a strong band at 250 nm associated to the charge transfer $O^{2-} \rightarrow Fe^{3+}$ (between oxygen *p* orbitals and the iron *d* electrons) of tetrahedral coordinated Fe^{3+} (Fe—O—Si) in the silica framework [22]. Besides the isomorphic substitution of silicon atoms by iron atoms, this band has been also assigned to the presence of iron oxide NPs in the mesopores when appeared with two extra absorption bands in the range 330–550 nm [22], as can be seen in the spectra of Fe-NPs (Fig. 2). Comparably, Fe-MCM-41 and Fe-ISS showed two additional peaks at ca. 330 and 550 nm. The band at 330 nm is associated to isolated extra-framework species in octahedral or pseudo-tetrahedral coordination while the presence of bands at wavelengths greater than 400 nm has been associated to iron oxide clusters and/or iron aggregates [23]. In fact, Fe-MCM-41

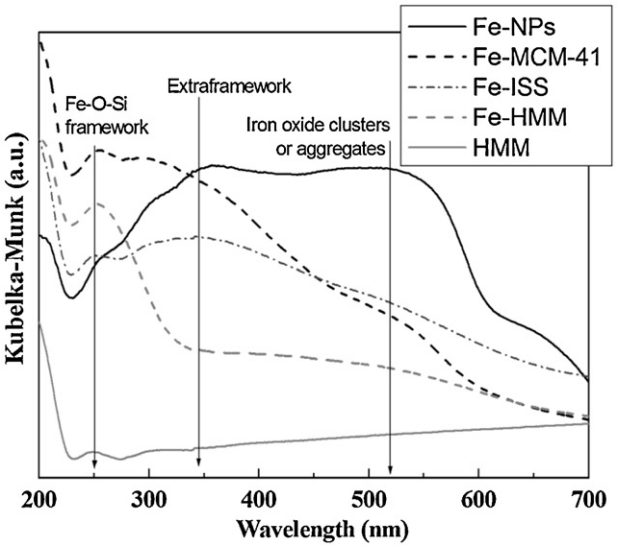

Fig. 2. DRUV spectra of Fe-MCM-41, Fe-HMM and Fe-ISS catalysts as compared with the DRUV spectra of iron oxide nanoparticles and HMM silica support.

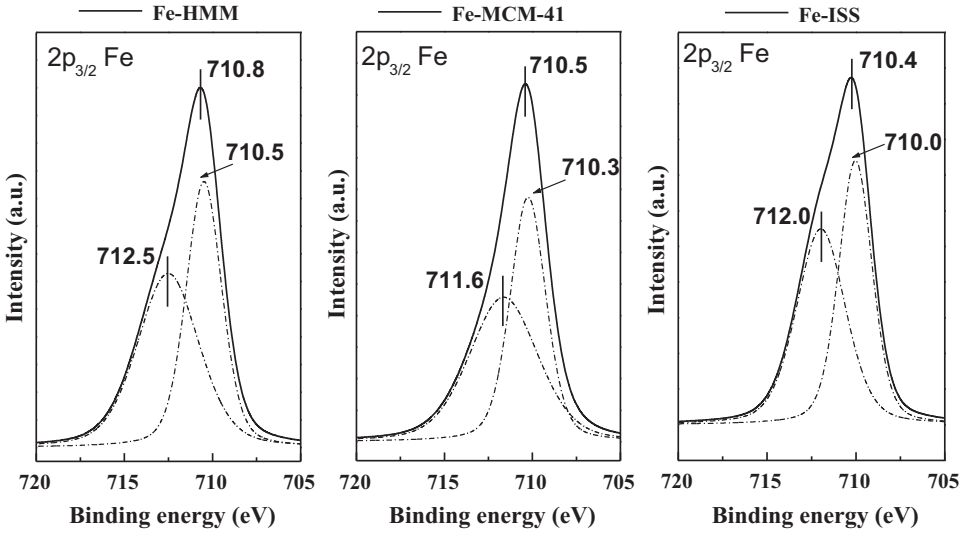

Fig. 3. XPS spectra of Fe-MCM-41, Fe-HMM and Fe-ISS silica materials.

possesses a more defined peak at 550 nm in comparison to the Fe-ISS solid, in good agreement with TEM results. The presence of those aggregates will correspond to a lower catalytic activity of the support [24], as shown below. Acidity measurements prove that, even if all solids show a low acidity (i.e. 28–41 μmol Py/g) due to the low amount of iron in their structures, Fe-HMM exhibited a slightly higher acidity to those of Fe-MCM-41 or Fe-ISS type materials (i.e. 41 μmol Py/g, vs. 33 and 28 μmol Py/g) respectively. The observed superior acidity could be due to the absence of iron in higher coordination as proved by DRUV analysis. Moreover, the presence of iron mostly tetrahedral coordinated leads to a higher catalytic activity as discussed in Section 4 of this manuscript.

XPS analyses show that iron oxide nanoparticles are a mixture of FeO and Fe_2O_3, being the Fe(III)/Fe(II) peak area ratio near to 1.11 for the three heterogeneous catalysts. XPS characteristic of Fe 2p2/3 spectra in nanoparticles is located around 707, 710 and 711 eV [25–27]. Peaks located near 711 eV and 710 eV can be clearly seen in Fig. 3 and they can be assigned to Fe^{3+} and Fe^{2+}, respectively. These peaks appear slightly displaced to higher energies in comparison to the reported spectra of iron oxide nanoparticles, probably due to the interaction between the NPs and the silica support [25–27]. The absence of the bands a lower energy, around 707 eV, points out the lack of Fe metal in the solids, which is consistent with both the high temperature used during the synthesis procedure and the lower reduction potential of Fe^{2+} (−0.4089 V) in comparison with other ions used for the nanoparticles synthesis, i.e. Ag+ (0.79 V) o Pd^{2+} (0.98 V). Wide-angle XRD patterns of the supported iron oxide nanoparticles confirm that the iron oxide nanoparticles incorporation does not significantly influence the structure of the materials. Anyway, no additional information about the iron species could be extracted due the low iron oxide loadings in the materials (Fig. 4a). Small-angle XRD patterns show that all solids maintained the 2-D hexagonal mesoporous arrangement of the silica supports, showing three distinctive (1 0 0), (1 1 0) and (2 0 0) X-ray diffractions peaks (see Fig. 4b and Table 1) [13,29–33]. Nitrogen adsorption/desorption isotherms of the mesoporous Fe-MCM-41, Fe-HMM and Fe-ISS materials prepared by a microwave-assisted approach and their corresponding pore size distributions are shown in Fig. 5a and b, respectively. For comparison purposes, the isotherms of the parent supports (samples denoted as MCM–41, HMM and ISS) are also included. All materials possessed type IV isotherms, typical of mesoporous materials, with a sharp nitrogen uptake at 0.35–0.45 P/P_0, which indicates a narrow pore size distribution (Fig. 5b). Based on these isotherms, the main textural parameters have been calculated and listed in Table 1. Average pore diameter was found to be ca. 3.0 nm in Fe-MCM-41 and Fe-HMM materials, typical for C_{16}TAB-templated materials [34] and slightly larger (3.40 nm) in the case of ISS type materials. This increase is probably due to the use of C_{18}TAB (with two more carbon atoms than C_{16}TAB), as structure directing agent during the material synthesis. The incorporation of iron oxide nanoparticles leads to a slight reduction in average pore size (c.a. 10%), pointing out a minor blocking of the porosity in the materials. This correlates well with the similar pore volumes and BET surface areas of Fe-materials with respect to their parent supports, due to the low amount of iron oxide nanoparticles present in the materials.

3.2. Catalytic tests

The catalytic activity of the materials was subsequently investigated in microwave-assisted redox (selective oxidation of benzyl alcohol) and acid (alkylation of toluene with benzyl chloride) catalyzed processes due to the dual redox-acid catalysis properties of iron oxide nanoparticles. This two test reactions were selected to study the different activities of the iron oxide nanoparticles supported on MCM-41 with different morphologies. Microwave-assisted reactions were selected on the basis of being an incredibly effective, safe, rapid, and highly reproducible way to perform autoclave experiments under strictly controlled processing conditions [35].

3.2.1. Benzyl alcohol oxidation

The activity of the Fe-MCM-41, Fe-HMM and Fe-ISS materials was initially evaluated in the selective oxidation of benzyl alcohol to benzaldehyde (Table 2, reaction (ii)). This reaction has been previously reported to be catalyzed by supported iron oxide nanoparticles on mesoporous aluminosilicate materials, in which a synergy Fe/Al was found to drive the reaction to high conversions(>50%) and selectivities (>85%) to benzaldehyde in very short times of reaction (typically 2 min) under microwave irradiation as compared to iron oxide nanoparticles supported on pure siliceous materials [24]. To the best of our knowledge, there are no reports on the effect of the catalyst morphology in the catalytic activity of the solids. Results included in Table 2 show that blank runs in the absence of catalyst or in the presence of MCM-41 type silica

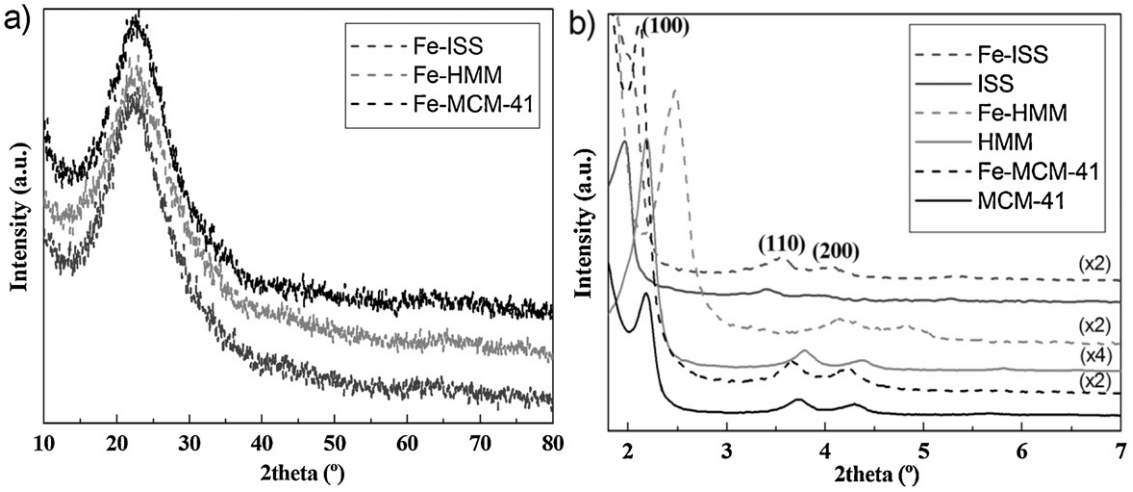

Fig. 4. XRD patterns of mesoporous silica materials: (a) wide-angle scan (10–80°) and (b) small-angle scan (1–10°). Spectra are shifted for clarity.

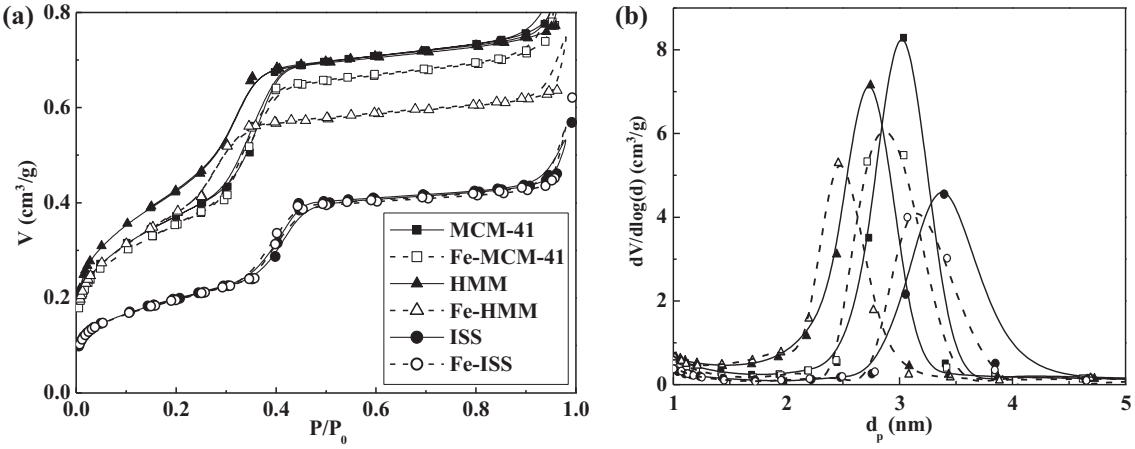

Fig. 5. Representative nitrogen adsorption/desorption isotherms at 77 K (a) and their corresponding pore size distribution (b) of the Fe-MCM-41, Fe-HMM and Fe-ISS catalysts, open symbols, as compared with the neat silica supports, fully symbols.

Table 2
Catalytic activity of the supported iron oxide nanoparticles in the microwave-assisted oxidation reaction of benzyl alcohol with hydrogen peroxide (i) and alkylation reaction of benzyl chloride with toluene (ii).

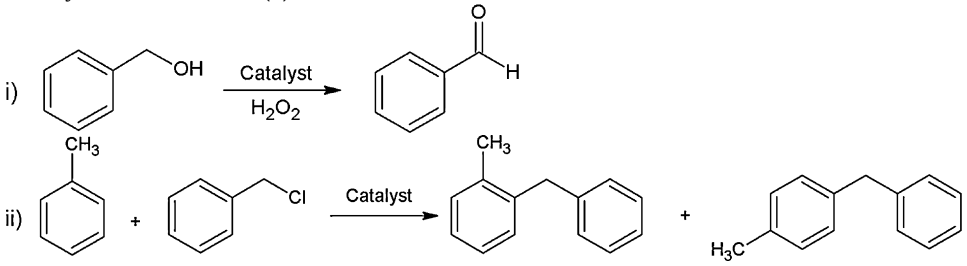

Catalyst	Oxidation reaction[a]		Alkylation reaction[b]		
	Conversion[c] (mol%)	Selectivity[c] (mol%)	Conversion[c] (mol%)	S ortho[c] (mol%)	S para[c] (mol%)
None	<5	>99	<2	56	44
MCM-41	<5	>99	<2	52	48
Fe-MCM-41	22	85	>99	45	55
Fe-HMM	32	95	>99	43	57
Fe-ISS	23	90	>99	42	58

[a] Reaction conditions: 2 mmol benzyl alcohol, 4 mmol H_2O_2 (0.4 ml, 30 wt% in water), 2 ml acetonitrile, 0.05 g catalyst, microwave irradiation 300 W, 3 min.
[b] Reaction conditions: 2 ml de toluene, 0.2 ml benzyl chloride, 0.025 g catalyst, microwave irradiation, 300 W, 3 min.
[c] Determined by GC; the difference to 100 corresponds to the formation of the only by product of the reaction (benzoic acid) upon over-oxidation of benzoic acid.

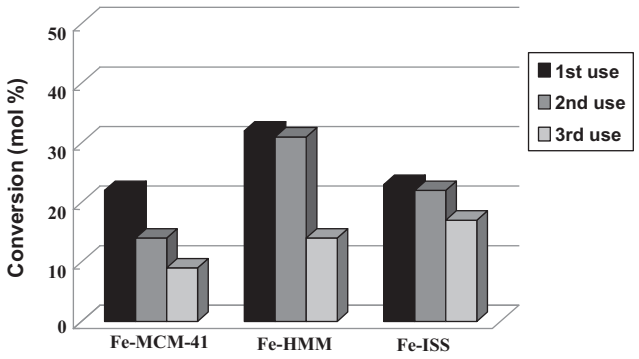

Fig. 6. Reuses of the Fe-MCM-41, Fe-HMM and Fe-ISS catalysts in the oxidation of benzyl alcohol. Reaction conditions: 2 mmol benzyl alcohol, 4 mmol H_2O_2 (0.4 ml, 30 wt% in water), 2 ml acetonitrile, 0.05 g catalyst, microwave irradiation 300 W, 3 min.

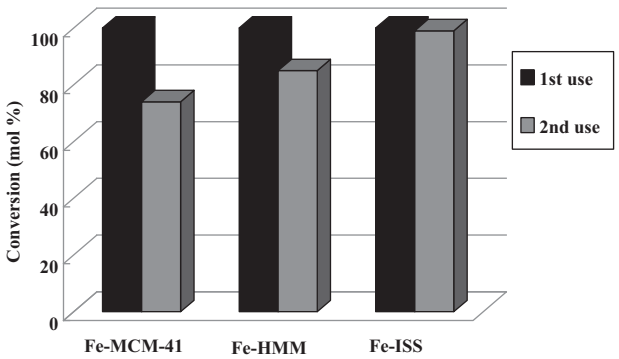

Fig. 7. Reuses of the of the Fe-MCM-41, Fe-HMM and Fe-ISS catalysts in the alkylation of benzyl chloride. Reaction conditions: 2 ml de toluene, 0.2 ml benzyl chloride, 0.025 g catalyst, microwave irradiation, 300 W, 3 min.

without active sites did not give any appreciable conversion of the starting material.

The conversion and selectivity obtained for the studied materials are similar to that reported by Luque et al. [24], typically between 20 and 40% conversion with high selectivity (>90%) to benzaldehyde. In all cases, H_2O_2 efficiency (calculated as the number of moles of product per consumed $H_2O_2 \times 100\%$) was found to be between 70 and 85%, depending on the catalyst employed in the reaction. Interestingly, Fe-HMM shows higher conversion than Fe-MCM-41 and Fe-ISS, despite the different amount of active sites. All the supports have shown a hexagonally ordered arrangement of the mesopores, typical of MCM-41 silica materials, and the difference between each of the morphologies is basically the shape and size of the particles forming the mesoporous materials. In the oxidation of benzyl alcohol, the activity and selectivity depends on the surface properties of iron oxide nanoparticles, although the acidity and a potential synergy Fe/Al is also likely to be present based on previous reports [24]. Among the possible difference on surface properties of the iron oxide nanoparticles due to their different sizes and the different incorporation on the silica supports, the observed difference in activity is then likely due to the smaller size of HMM particles in the supports (diameter around 80 nm) in comparison with ISS particles (diameter around 250 nm) and MCM-41 materials (particles show sizes of several hundred of nanometers). As previously reported by Suzuki et al. [36], by decreasing the particle size, the surface/volume ratio increases which means that the smaller silica particles have higher external surface for the iron oxide nanoparticles dispersion and, consequently, the catalytic activity could be improved. Moreover, while most of the iron species remained in the silica framework in Fe-HMM catalyst, iron oxide NP aggregates have been detected by DRUV and TEM analyses, which could also contribute to a different catalytic activity of the helical catalyst [24]. The activity for Fe-ISS materials was similar to that achieved by Fe-MCM-41, even though Fe-ISS possesses twice as much as iron loading and BET surface area. This fact suggests that the surface areas of materials are not a determining parameter for the catalytic activity of the materials. XRD, XPS and UV results show both samples should have similar iron oxides, thus the oxidation results indicate that the microwave-assisted catalyst preparation is more suitable to ISS with respect to MCM-41 morphology.

To test the reusability of as-synthesized catalysts, materials were filtered off after the first microwave-assisted oxidation reaction and re-loaded into a microwave tube with fresh reagents to evaluate their catalytic activity. This process was carried out twice. Surprisingly, the reusability of the solids was also strongly dependent on the morphology of the support (Fig. 6) with Fe-HMM providing the highest conversion after its second use (around 30 mol%), although its activity decreases around 50% after the third use. The reason for this is currently not well understood but seems to be related to a potential sintering of the iron oxide species after each cycle that could lead to larger agglomerates of lower activity. TEM studies will follow these explanations to ascertain the nature of the deactivation phenomena. As expected, Fe-MCM-41 solid showed a poor reusability probably due to the presence of iron oxide nanoparticles in the external surface of the silica network as well as the larger MCM-41 particle size. Interestingly, Fe-ISS type silica also maintained its activity after the second use with only a slight decrease after the third use, showing that this material, although less active as compared to Fe-HMM, could be an interesting candidate for continuous flow oxidations under relatively high temperatures and pressures similar to those utilized under microwave irradiation. In all cases, the structure and morphology of the porous materials was preserved after reuse as shown in Fig. 1d for Fe-HMM. Materials were also stable under the investigated conditions, with no leaching detected after several uses as determined by ICP-MS.

3.2.2. *Alkylation of toluene with benzyl chloride*

The second test reaction studied was the alkylation of toluene with benzyl chloride (reaction (ii) in Table 2). This reaction has been carried out following the optimized conditions reported by Gracia et al. [21].

The results shown in Table 2 point out that 3 min of reaction time under microwave irradiation are sufficient to provide full conversion of the starting materials in the systems with a similar selectivity for both *ortho*- and *para*-substituted products. Shorter reaction times only provided minor differences in activity of the mesoporous catalysts which indicate (in contrast with the oxidation results) that there is no significant influence of the morphology of the support for this particular reaction under the investigated conditions. However, interesting differences were observed in the reusability experiments (Fig. 7). Fe-MCM-41 showed again poorer reusability than Fe-HMM and Fe-ISS, which achieved similar catalytic activities after their second use. These findings confirmed the better and more stable interaction of iron oxide nanoparticles on HMM and ISS supports than on conventional MCM-41 materials. In all cases, no Fe content was detected by ICP-MS, ruling out the possibility of Fe leaching in the materials under the investigated conditions.

4. Conclusions

Three different mesoporous silicas with distinctive morphologies have been prepared and utilized as supports for iron oxide nanoparticles. The morphology of the support was found to influences both nanoparticle dispersion and structure as well as the

accessibility of active sites. All mesoporous silica materials studied exhibited good and versatile catalytic activities in two different processes including the selective oxidation of benzyl alcohol to benzaldehyde (redox process) and alkylation of toluene with benzyl chloride (acid catalyzed process). Important differences were observed for different morphologies, with activities of Fe-HMM and Fe-ISS comparable and/or superior in all cases to those of iron oxide nanoparticles on conventional MCM-41. Reusability of the solids was observed to be somewhat dependent on the morphology of the support, with Fe-MCM-41 being less reusable as compared to Fe-HMM and Fe-ISS.

Acknowledgments

J.G.M. and R.L. gratefully acknowledge funding under project CTQ2011-28954-C02-01(02) (MICINN) from the Spanish MICINN. R.L. is also grateful for financial support via the concession of a RyC contract (RYC 2009 04199) and funding under the project P10-FQM-6711 (Consejeria de Ciencia e Innovacion, Junta de Andalucia). E.S. is grateful for financial support under the JdC program (ref. JCI 2008–2165) and from GV (ref. BEST2011/223). The authors are also grateful to the Technical Services of the University of Alicante (SSTTi).

References

[1] J.H. Clark, Green Chem. 1 (1999) 1–8.
[2] J.H. Clark, G.A. Kraus, Green Chemistry Series Book, RSC Publishing, Cambridge, 2009.
[3] A. Balu, J. Campelo, A.I. Carrillo, N. Linares, J. Garcia-Martinez, E. Serrano, R. Luque, A.A. Romero, Palladium: Compounds, Products and Applications, NOVA Science Publishing, New York, 2011 (Chapter 4).
[4] C.A. Mirkin, Small 1 (2005) 14–16.
[5] G. Schmid, V. Maihack, F. Lantermann, S. Peschel, J. Chem. Soc., Dalton Trans. (1996) 589–595.
[6] A. Doyle, S.K. Shaikhutdinov, S.D. Jackson, H.J. Freund, Angew. Chem. Int. Ed. 42 (2003) 5240–5243.
[7] J.A. Dahl, B.L.S. Maddux, J.E. Hutchinson, Chem. Rev. 107 (2007) 2228–2269.
[8] N. Toshima, Macromol. Symp. 204 (2003) 219–226.
[9] D. Astruc, F. Lu, J.R. Aranzaes, Angew. Chem. Int. Ed. 44 (2005) 7852–7872.
[10] R.J. White, R. Luque, V. Budarin, J.H. Clark, D.J. Macquarrie, Chem. Soc. Rev. 38 (2009) 481–494.
[11] J.M. Campelo, T.D. Conesa, M.J. Gracia, M.J. Jurado, R. Luque, J.M. Marinas, A.A. Romero, Green Chem. 10 (2008) 853–858.
[12] (a) N. Linares, E. Serrano, M. Rico, A.M. Balu, E. Losada, R. Luque, J. García-Martínez, Chem. Commun. 47 (2011) 9024–9036;
(b) N. Linares, A.E. Sepulveda, M.C. Pacheco, J.R. Berenguer, E. Lalinde, C. Najera, J. Garcia-Martinez, New J. Chem. 35 (2011) 225–234;
(c) J. Garcia-Martinez, N. Linares, S. Sinibaldi, E. Coronado, A. Ribera, Microporous Mesoporous Mater. 117 (2009) 170–177;
(d) A.I. Carrillo, J. Garcia Martinez, R. Llusar, E. Serrano, I. Sorribes, C. Vicent, A. Vidal-Moya, Microporous Mesoporous Mater. 151 (2012) 380–389.
[13] (a) A.I. Carrillo, N. Linares, E. Serrano, J. Garcia-Martinez, Mater. Chem. Phys. 129 (2011) 261–269;
(b) A.I. Carrillo, E. Serrano, R. Luque, J. Garcia-Martinez, Chem. Commun. 46 (2010) 5163–5165;
(c) A.I. Carrillo, E. Serrano, J.C. Serrano, R. Luque, J. Garcia-Martinez, Appl. Catal. A 435 (2012) 1–9.
[14] C.E. Fowler, D. Khushalani, B. Lebeau, S. Mann, Adv. Mater. 13 (2001) 649–652.
[15] J. Garcia-Martinez, P. Brugarolas, S. Dominguez-Dominguez, Microporous Mesoporous Mater. 100 (2007) 63–69.
[16] Y. Han, L. Zhao, J.Y. Ying, Adv. Mater. 19 (2007) 2454–2459.
[17] F. Kleitz, U. Wilczok, F. Schüth, F. Marlow, Phys. Chem. Chem. Phys. 3 (2001) 3486–3489.
[18] C. Gonzalez-Arellano, J.M. Campelo, D.J. Macquarrie, J.M. Marinas, A.A. Romero, R. Luque, ChemSusChem 1 (2008) 746–750.
[19] C.C. Chusuei, M.A. Brookshier, D.W. Goodman, Langmuir 15 (1999) 2806–2808.
[20] M. Kruk, M. Jaroniec, J.M. Kim, R. Ryoo, Langmuir 15 (1999) 5279–5284.
[21] M.J. Gracia, E. Losada, R. Luque, J.M. Campelo, D. Luna, J.M. Marinas, A.A. Romero, Appl. Catal. A 349 (2008) 148–155.
[22] (a) B. Echchahed, A. Moen, D. Nicholson, L. Bonneviot, Chem. Mater. 9 (1997) 1716–1719;
(b) P. Selvam, S.E. Dapurkar, S.K. Badamali, M. Murugasan, H. Kuwano, Catal. Today 68 (2001) 69–74;
(c) S.E. Dapurkar, S.K. Badamali, P. Selvam, Catal. Today 68 (2001) 63–68;
(d) T. Abe, Y. Tachibana, T. Uematsu, M. Iwamoto, J. Chem. Soc., Chem. Commun. (1995) 1617–1618.
[23] (a) Y. Sun, S. Walspurger, J.P. Tessonnier, B. Louis, J. Sommer, Appl. Catal. A 300 (2006) 1–7;
(b) Y. Li, Z. Feng, H. Xin, F. Fan, J. Zhang, E.J.M. Hensen, R.A. van Santen, Q. Yang, C. Li, J. Phys. Chem. B 110 (2006) 26114–26121.
[24] A.M. Balu, A. Pineda, K. Yoshida, J.M. Campelo, P.L. Gai, R. Luque, A.A. Romero, Chem. Commun. 46 (2010) 7825–7827.
[25] T. Tsoncheva, S. Areva, M. Dimitrov, D. Paneva, I. Mitov, M. Linden, C. Minchev, J. Mol. Catal. A 246 (2006) 118–127.
[26] C.T. Wang, S.H. Ro, Appl. Catal. A 285 (2005) 196–204.
[27] B.M. Weckhuysen, D. Wang, M.P. Rosynek, J.H. Lunsford, J. Catal. 175 (1998) 347–351.
[28] J.M. Campelo, D. Luna, R. Luque, J.M. Marinas, A.A. Romero, J.J. Calvino, M.P. Rodriguez-Luque, J. Catal. 230 (2005) 327–338.
[29] W. Hammond, E. Prouzet, S.D. Mahanti, T.J. Pinnavaia, Microporous Mesoporous Mater. 27 (1999) 19–25.
[30] B. Marler, U. Oberhagemann, S. Vortmann, H. Gies, Microporous Mater. 6 (1996) 375–383.
[31] M.H. Lim, A. Stein, Chem. Mater. 11 (1999) 3285–3295.
[32] P. Ferreira, I.S. Goncalves, F.E. Kuhn, M. Pillinger, J. Rocha, A. Thursfield, W.M. Xue, G. Zhang, J. Mater. Chem. 10 (2000) 1395–1401.
[33] M. Jia, A. Seifert, W.R. Thiel, Chem. Mater. 15 (2003) 2174–2180.
[34] H. Li, F. Zhang, H. Yin, Y. Wan, Y. Lu, Green Chem. 9 (2007) 500–505.
[35] C.O. Kappe, B. Pieber, D. Dallinger, Angew. Chem. Int. Ed. (2012), http://dx.doi.org/10.1002/anie.201204103.
[36] T.M. Suzuki, T. Nakamura, K. Fukumoto, M. Yamamoto, Y. Akimoto, K. Yano, J. Mol. Catal. A 280 (2008) 224–232.